

# Dynamic nonlinear behavior of torsional resonators in MEMS

A Caspani<sup>1</sup>, C Comi<sup>2</sup>, A Corigliano<sup>2</sup>, G Langfelder<sup>1</sup>, V Zega<sup>2</sup> and S Zerbini<sup>3</sup>

<sup>1</sup> Department of Electronics, Information and Bioengineering, Politecnico di Milano, 20133 Milan, Italy

<sup>2</sup> Department of Civil and Environmental Engineering, Politecnico di Milano, 20133 Milan, Italy

<sup>3</sup> AMS group, STMicroelectronics, 20010 Cornaredo, Milan, Italy

E-mail: [claudia.comi@polimi.it](mailto:claudia.comi@polimi.it)

Received 30 June 2014

Accepted for publication 11 July 2014

Published 22 August 2014

## 1. Introduction

Torsional microresonators have applications in a number of microdevices, including gyroscopes and resonant accelerometers [1–4], magnetometers [5], mass detection devices [6], and micro-mirrors [7]. In particular, when the devices are fabricated through surface micro-machining, due to the planar geometry, the out-of-plane modes are seldom of bending type, as e.g. in [8], and more frequently torsional modes are activated. The study of torsional resonators, both in the linear and nonlinear ranges, is therefore needed in order to properly design such devices. While a significant amount of research has been devoted to the nonlinear behavior of bending micro-resonators (see e.g. [9–12]), very few works have focused on the nonlinear behavior of torsional micro-resonators, [13]. The purpose of this work is to model the nonlinear behavior of an electrostatically actuated torsional resonator, studying in detail the effect of imperfections due to the fabrication process and the influence of the geometry of the resonating mass.

In particular, we consider the structure of the resonant accelerometer recently proposed in [3], fabricated using the THELMA© surface micromachining process from STMicroelectronics [14], see figures 1 and 2. Two torsional

resonators, labeled A and B in figure 1, consisting of a square mass and two folded torsional springs attached to the proof mass, allow for the differential sensing of the acceleration. Driving and sensing of the resonators is obtained through two parallel electrodes attached to the substrate, as shown by dashed lines in figure 2 and also represented in figure 3. When an external out-of-plane acceleration is applied, the proof mass tilts and the frequency of the resonators change due to the variation of the electric stiffness induced by the gap variation.

To obtain a high sensitivity the mechanical torsional stiffness of the resonators should be low but this can result in nonlinear dynamic behavior which is studied in this paper.

The paper is organized as follows. In section 2, Hamilton's principle is formulated for the mechanical description of nonlinear oscillations of an electrostatically actuated torsional resonator. In section 3, Hamilton's principle is used as a basis for a one-degree-of-freedom formulation and analytical solutions are obtained. Section 4 discusses the influence of the geometry of the resonator and of the fabrication imperfections on the nonlinear behavior. The experimental results obtained both in the linear and nonlinear regimes on the resonators of the resonant out-of-plane accelerometer [3] are presented and discussed in section 5. The experimental data concerning the

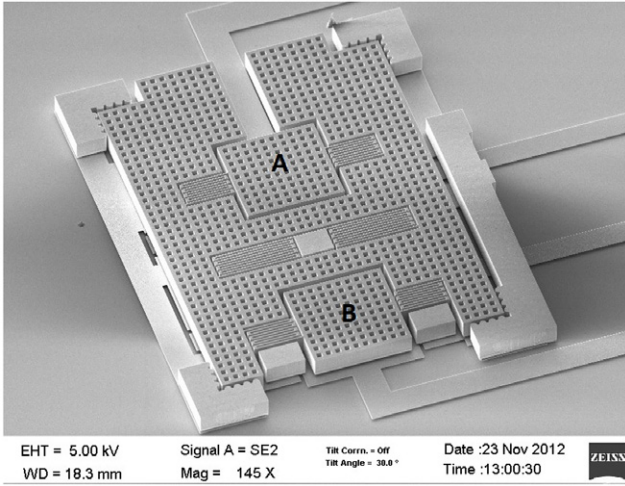


**Figure 1.** SEM image of the z-axis accelerometer with two torsional resonators, labeled A and B, attached to the proof mass.

linear regime are first used for the identification of the quality factor  $Q$  and of fabrication imperfections with respect to the expected etching, then the results concerning the nonlinear regime are compared with the theoretical predictions. A good agreement is obtained.

## 2. Hamilton's principle applied to an electrostatically actuated torsional resonator

Let us focus on the scheme of an ideal electrostatically actuated torsional resonator, as shown in figures 3 and 4. A mass of in-plane dimensions  $2b \times L$  and out-of-plane thickness  $t$  is connected to the device by two torsional springs which allow for its out-of-plane rotation  $\theta(x, t)$  (counterclockwise positive). The mass is considered to be rigid while the deformable elements or 'springs' are thin beams of in-plane width  $s$ , out-of-plane thickness  $t$  and length  $l$ . Usually these springs are folded into  $n$  folds of length  $l/n$  in order to obtain a torsional stiffness lower than the bending stiffness. The geometric nominal data of the resonators of the fabricated accelerometer are listed in table 1. Note that the in-plane dimensions include the nominal over-etch of  $0.35 \mu\text{m}$ , which is the deviation between the designed masks and the effective dimensions of the suspended parts.

When in the rest position, the mass is at distance  $g_0$  from both electrodes (see figure 3). The sensing electrode is usually connected to a virtual ground at zero voltage while the mass is kept at the polarization fixed voltage  $V_p$ . By applying a small variable voltage  $v_a(t)$  to the driving electrode the mass is electrostatically actuated and can dynamically vibrate.

The equations governing the torsional resonator dynamics can be obtained making use of Hamilton's variational principle [15]. This principle states that the sum of the time variation of the difference between kinetic and potential energies and the work done by the non-conservative forces over any time interval  $t_1$  and  $t_2$  equals zero, for any varied path  $\delta\theta$  from time  $t_1$  and  $t_2$  with  $\delta\theta(t_1) = \delta\theta(t_2) = 0$ :

$$\int_{t_1}^{t_2} \delta[\mathcal{T}(\dot{\theta}) - \mathcal{V}(\theta)]dt + \int_{t_1}^{t_2} \delta W_{nc}(t)dt = 0 \quad (1)$$

$\mathcal{T}$  being the kinetic energy,  $\mathcal{V}$  the potential energy and  $W_{nc}$  the virtual work of non conservative forces. The Lagrange functional  $\mathcal{L}$  is defined as  $\mathcal{L} = \mathcal{T} - \mathcal{V}$ .

The kinetic energy is expressed as:

$$\mathcal{T}(\dot{\theta}) = 2\frac{1}{2} \int_0^l \rho J_p \dot{\theta}^2 dx + \frac{1}{2} \rho J_{\text{mass}} \dot{\theta}^2 \quad (2)$$

where  $\rho$  is the mass density,  $J_p$  is the polar moment of inertia of a single spring,  $\rho J_{\text{mass}}$  is the centroidal mass moment of inertia of the rigid mass and  $\theta = \theta(l, t)$ .

The potential energy  $\mathcal{V}$  is given by the difference of the elastic deformation energy  $\Omega_e$  of the two springs and the work of external loads which, in the present case, coincides with the work of electrostatic loads  $W_{\text{elec}}(\theta)$

$$\begin{aligned} \mathcal{V}(\theta) &= \Omega_e(\theta) - W_{\text{elec}}(\theta) \\ &= 2\frac{1}{2} \left( \int_0^l E \Gamma (\theta'')^2 dx + \int_0^l G J_t (\theta')^2 dx \right) - W_{\text{elec}} \end{aligned} \quad (3)$$

where  $G$  is the shear elasticity modulus,  $\Gamma$  is the warping stiffness,  $J_t$  is the torsional momentum of inertia,  $E$  is the Young's modulus and  $\theta'$  is the first derivative of  $\theta$  with respect to the coordinate  $x$ . Note that in (3), in agreement with experimental evidence [14], a linear elastic behavior for silicon is assumed. Moreover, geometrical effects are not included as they are completely negligible in the range of rotation angles that the resonator can experience. Thus the deformation energy  $\Omega_e$  is quadratic and leads to a linear mechanical stiffness term in the equation of motion. On the contrary, nonlinear terms arise from the electrostatic loads.

The work of electrostatic loads  $W_{\text{elec}}(\theta)$  is defined as

$$W_{\text{elec}}(\theta) = \int_0^\theta T_e(\alpha) d\alpha \quad (4)$$

where  $T_e$  is the electrostatic torque acting on the proof mass which can be calculated for the actuation scheme of figure 3 and reads

$$\begin{aligned} T_e &= \int_c^b -\frac{1}{2} \frac{\epsilon_0 L}{(g_0 + \theta y)^2} (V_p - v_a)^2 y dy \\ &+ \int_{-b}^{-c} -\frac{1}{2} \frac{\epsilon_0 L}{(g_0 + \theta y)^2} V_p^2 y dy. \end{aligned} \quad (5)$$

The dependence of the electrostatic work on the mass rotation  $\theta$  can be approximated by a polynomial expansion around  $\theta = 0$  up to the fourth order; under the hypothesis that the actuation voltage is small with respect to the polarization voltage  $|v_a| \ll V_p$  the following expression is obtained:

$$\begin{aligned} W_{\text{elec}}(\theta) &= \frac{\epsilon_0 L}{2} \left[ \frac{V_p v_a}{g_0^2} (b^2 - c^2) \theta + \frac{2V_p^2}{3g_0^3} (b^3 - c^3) \theta^2 \right. \\ &\left. + \frac{2V_p^2}{5g_0^5} (b^5 - c^5) \theta^4 \right]. \end{aligned} \quad (6)$$

Finally, the virtual work of the non-conservative forces  $W_{nc}$  is here given by viscous damping and can be expressed as:

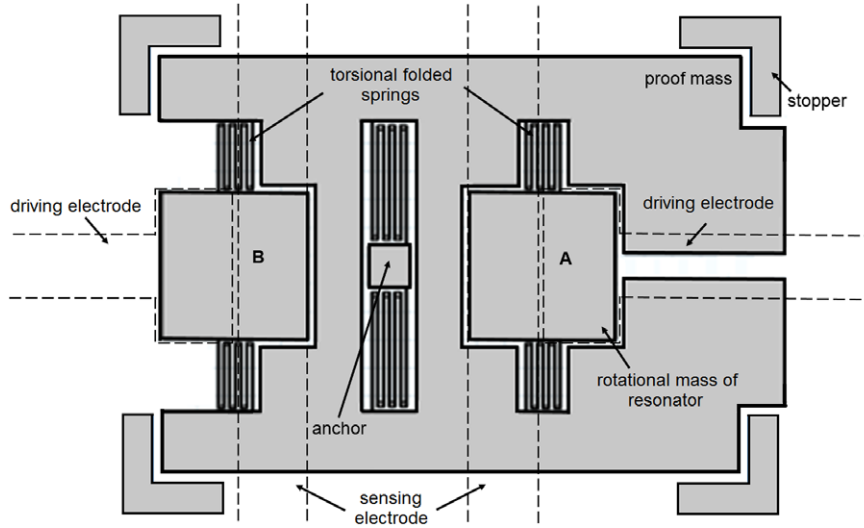


Figure 2. Top view scheme of the  $z$ -axis accelerometer.

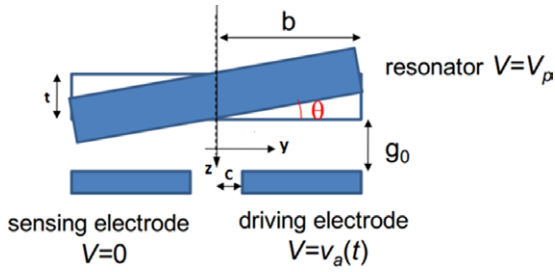


Figure 3. Side-view scheme of the torsional resonator with electrostatic actuation;  $V_p$  = fixed polarization voltage,  $v_a(t)$  = oscillating driving voltage,  $g_0$  = out-of-plane gap.

Table 1. Parameters of a single torsional resonator.

Parameter	Value	Units
$L$	105.00	$\mu\text{m}$
$2b$	105.00	$\mu\text{m}$
$l$	341.40	$\mu\text{m}$
$s$	2.00	$\mu\text{m}$
$t$	22.00	$\mu\text{m}$
$g_0$	1.80	$\mu\text{m}$
$J_t$	58.67	$\mu\text{m}^4$
$J_{\text{mass}}$	$2.33 \cdot 10^8$	$\mu\text{m}^5$
$\Gamma$	123.98	$\mu\text{m}^6$
$E$	$1.5 \cdot 10^5$	MPa
$G$	$6.15 \cdot 10^4$	MPa

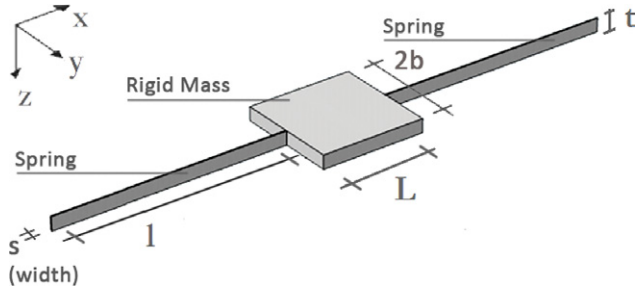


Figure 4. Geometry of the torsional resonator.

$$W_{nc} = \frac{1}{2} \int_0^l b^* \dot{\theta}^2 dx \quad (7)$$

where  $b^*$  is a viscous damping coefficient.

The governing equations of the torsional resonator dynamics and the relevant boundary conditions can be found by enforcing Hamilton's principle as in equation (1), taking into account equations (2)–(7).

### 3. One-degree-of-freedom approximation

A numerical solution for the torsional oscillation can be obtained expressing  $\theta$  in terms of a set of  $n$  generalized

coordinate  $Z_i(t)$  multiplied by known space functions  $\Phi_i(x)$ , substituting it into the kinetic and potential energies and into the virtual work of nonconservative forces and using the Hamilton's principle to obtain the Lagrange equations of motion:

$$\frac{d}{dt} \frac{\partial \mathcal{L}}{\partial \dot{Z}_i} - \frac{\partial \mathcal{L}}{\partial Z_i} = Q_{nc,i} \quad i = 1 \dots n, \quad (8)$$

$Q_{nc,i}$  being the generalized non conservative force. In the spirit of the Rayleigh method a single generalized variable  $Z(t)$  can be introduced and the approximate solution for the torsional oscillation can be searched in the form:

$$\theta(x, t) = Z(t) \Phi(x), \quad (9)$$

$\Phi(x)$  being the eigen-function of the linear problem, corresponding to a quadratic approximation of the electrostatic work in equation (6). Normalizing the eigenfunction so that  $\Phi(l) = 1$ , one can interpret the generalized variable as the rotation of the rigid mass

$$\Theta(t) = \theta(l, t) = Z(t) \Phi(l) = Z(t). \quad (10)$$

Relations (9) and (10) are now substituted into (8) thus obtaining the following equation of motion for a one-degree-of-freedom torsional oscillator

$$j\ddot{\Theta} + B\dot{\Theta} + k_1\Theta + k_3\Theta^3 = M(t) \quad (11)$$

with

$$j = 2 \int_0^l \rho J_p \Phi^2 dx + \rho J_{\text{mass}}, \quad (12)$$

$$k_1 = k_{m1} + k_{e1}, \quad (13)$$

$$k_{m1} = 2 \int_0^l E \Gamma (\Phi'')^2 dx + 2 \int_0^l G J_t (\Phi')^2 dx, \quad (14)$$

$$k_{e1} = - \frac{2\epsilon_0 L}{g_0^3} V_p^2 \left( \frac{b^3}{3} - \frac{c^3}{3} \right), \quad (15)$$

$$k_3 = k_{e3} = - \frac{4\epsilon_0 L}{g_0^5} V_p^2 \left( \frac{b^5}{5} - \frac{c^5}{5} \right), \quad (16)$$

$$M(t) = \frac{\epsilon_0 L}{g_0^2} V_p v_a(t) \left( \frac{b^2}{2} - \frac{c^2}{2} \right), \quad (17)$$

$$B = \int_0^l b^* \Phi^2 dx. \quad (18)$$

In equation (11)  $j$  and  $B$  are the effective mass and damping coefficient of the resonator,  $k_{e1}$  and  $k_{e3}$  are the first- and third-order term of the electrostatic stiffness,  $k_{m1}$  is the elastic stiffness and  $M(t)$  is the external torque applied to sustain the oscillation.

Equation (11) describes the motion of a nonlinear oscillator and it is known as the Duffing oscillator equation for a single-degree-of-freedom system.

Due to the geometry of the torsional springs, the ratio  $\frac{E\Gamma}{GJ_t l^2}$  is very small and the contribution of the secondary torsional stiffness can be neglected. Therefore all terms in (11)–(18) can be computed choosing for  $\Phi(x)$  the eigen-function of the linear torsional oscillator, normalized so that  $\Phi(l) = 1$ , i.e.:

$$\Phi(x) = \frac{1}{\sin\left(\sqrt{\frac{J_p}{J_{\text{mass}} l}} l\right)} \sin\left(\sqrt{\frac{J_p}{J_{\text{mass}} l}} x\right). \quad (19)$$

Substituting (19) into (14), under the hypothesis of  $\alpha l = \sqrt{\frac{J_p}{J_{\text{mass}} l}} l$  small, the first-order term of mechanical elastic stiffness can be expressed as

$$k_{m1} = 2GJ_t \alpha^2 \frac{1}{\sin(\alpha l)^2} \left( \frac{l}{2} + \frac{\sin(2\alpha l)}{4\alpha} \right) \approx \frac{2GJ_t}{l} \quad (20)$$

that is the linear torsional stiffness of two elastic beams. When the springs are folded, the mechanical stiffness should be numerically computed, e.g. by a finite element analysis as will be done in section 5.

The solution of equation (11) can be obtained from series of successive approximations, see [16], as

$$\Theta = \Theta^{(1)} + \Theta^{(2)} + \Theta^{(3)} \quad (21)$$

where

$$\Theta^{(1)} = A \cos(\omega t), \quad (22)$$

$$\Theta^{(2)} = 0, \quad (23)$$

$$\Theta^{(3)} = - \frac{A^3 k_3}{32 k_1} \cos(3\omega t). \quad (24)$$

In (22)–(24)  $A$  is the oscillation amplitude and  $\omega$  is the actual value of the angular frequency, which differs from the reference value of the linear case  $\omega_0 = \sqrt{\frac{k_1}{j}}$  and, under the assumption of very high  $Q$ -factor, is expressed as:

$$\omega = \omega_0 \left[ 1 + \frac{3 k_3}{8 k_1} A^2 \right]. \quad (25)$$

Nonlinearity also affects the forced oscillation of the system. Considering a harmonic driving term  $M(t) = \bar{M} \cos(\gamma t)$ , of frequency  $\gamma$  close to the natural frequency, one obtains a relation between the amplitude  $\bar{M}$  and the frequency  $\gamma$  of the driving force and the amplitude  $A$  of the forced vibration of the beam:

$$\left( \frac{\bar{M}}{k_1} \right)^2 = \left( 2 \left( 1 - \frac{\gamma}{\omega_0} \right) A + \frac{3 k_3}{4 k_1} A^3 \right)^2 + \left( \frac{B}{j\omega_0} A \right)^2. \quad (26)$$

### 3.1. Quality factor

The quality factor is a key parameter for the performance of resonating devices. For the one-degree-of-freedom torsional oscillator, it is related to the equivalent damping coefficient through the equation

$$Q = \frac{j\omega}{B} \quad (27)$$

In the case of rarefied air conditions, the classical continuum gas flow theory does not provide correct predictions of gas damping. The limit of validity for the continuum gas flow theory is conventionally expressed in terms of the Knudsen number, i.e. of the ratio between the mean free path of gas molecules  $\lambda$  and the characteristic length of the flow  $L_c$ :

$$K_n = \frac{\lambda}{L_c} = \frac{k_B T}{\sqrt{2} \pi d_{\text{gas}}^2 p L_c} \quad (28)$$

where  $k_B = 1.38 \times 10^{-23} \text{ JK}^{-1}$  is Boltzmann's constant,  $T$  is the temperature [K],  $d_{\text{gas}}$  is the diameter of the gas molecule and  $p$  is the pressure. For  $K_n > 10$  the free molecule regime is entered. The experimental results discussed in the following are obtained in this regime. In fact they refer to a device packaged at  $p = 10^2 \text{ Pa}$ , corresponding to the mean free path at room temperature  $\lambda = 63 \text{ }\mu\text{m}$ ; in that device the characteristic length of the flow can be assumed equal to the gap between the resonators and the substrate  $g_0 = 1.8 \text{ }\mu\text{m}$ , leading to  $K_n = 35$ . Several models have been proposed in the literature to compute the quality factor in the free molecule regime. In particular in [17], the closed-form expression obtained in [18] for an oscillating rectangular plate is adapted to the case of a

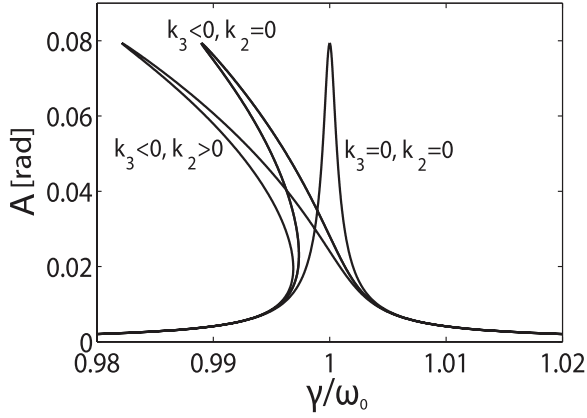


**Figure 5.** Theoretical prediction of spectral response of the torsional resonator with and without the third- and second-order term of the electrostatic stiffness.

tilting resonator. Using the notation introduced in figure 4, the quality factor can be expressed as

$$Q_{FM} = (2\pi)^{\frac{3}{2}} \rho t \omega \frac{g_0}{4b + 4L} \sqrt{\frac{RT}{M_m}} \frac{1}{p} \quad (29)$$

where  $R$  is the ideal gas constant and  $M_m$  is the gas molar mass.

It should be noted that the above expression holds for a plate without holes. The presence of holes reduces the dissipation and results in a higher quality factor. A numerical analysis is required in this case, as discussed in detail in [19].

#### 4. Discussion on the nonlinear behavior

As already observed, in the considered torsional resonators, the nonlinear behavior is only due to the electrostatic stiffness term. Since  $k_{e3}$  is always negative, a ‘soft spring’ effect is observed leading to a resonance curve being bent backward, see figure 5.

To reduce  $k_{e3}$  and hence nonlinearities one has to lower the polarization voltage or reduce the size of the electrodes. However the operating voltage is often fixed in a given range in order to obtain the required sensitivity of the device. An alternative way to reduce nonlinearities and enlarge the linear range of functioning is to properly design the oscillating mass.

In particular the ratio  $\frac{k_{e3}}{k_{e1}}$  decreases if the aspect ratio of the mass  $\frac{L}{2b}$  increases. This effect is shown in figure 6 where the ratio of the linear and the third-order term of the electrostatic torque is plotted for different geometries of the resonating mass maintaining the area constant.

It is evident that by increasing  $\frac{L}{2b}$  the third-order contribution becomes smaller and the ratio between the linear contribution and the third order is greater than one up to higher rotation angles. It is therefore possible to increase or decrease nonlinearities varying only geometrical parameters. The torsional resonators of the  $z$ -axis accelerometer [3], which will be analyzed in the following section, have a square mass  $\left(\frac{L}{2b} = 1\right)$ .

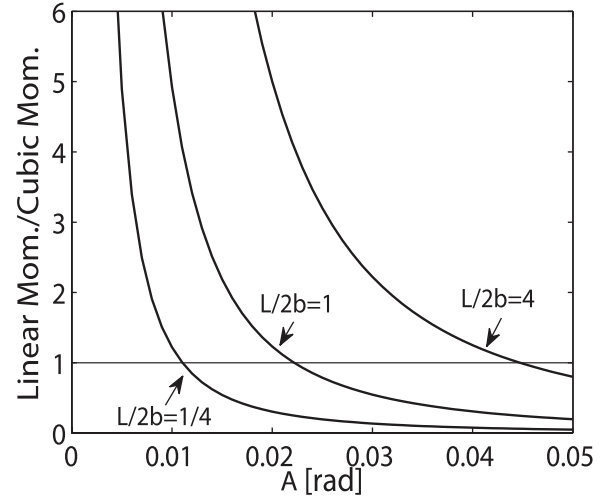


**Figure 6.** Ratio of linear and third-order term of the electrostatic torque applied to the torsional resonator for different geometries of the proof mass. The area of the proof mass is maintained constant for all the different configurations.

During its functioning, the whole proof mass of the accelerometer tilts and its inclination  $\beta$  must be considered in the nonlinear analysis of the resonators. In fact, the inclination of the proof mass of the accelerometer causes a variation of the rest gap  $g_0$  below the two torsional resonators and, consequently, the external torque applied assumes the expression:

$$T_e = \int_c^b -\frac{1}{2} \frac{\epsilon_0 L}{(\hat{g}_0 + \Theta y + \beta y)^2} (V_p - v_a)^2 y dy + \int_{-b}^{-c} -\frac{1}{2} \frac{\epsilon_0 L}{(\hat{g}_0 + \Theta y + \beta y)^2} V_p^2 y dy \quad (30)$$

where  $\hat{g}_0 = g_0 + \eta\beta$ ,  $\eta$  denoting the position of the resonator with respect to the rotation axis of the accelerometer.

In that case the equation of motion becomes:

$$j\ddot{\Theta} + B\dot{\Theta} + k_1\Theta + k_2\Theta^2 + k_3\Theta^3 = M(t) \quad (31)$$

where  $k_2 = k_{e2}$  is the second-order term of the electrostatic stiffness due to the inclination of the proof mass of the  $z$ -axis accelerometer and can be expressed as:

$$k_{e2} = f(\zeta)|_{\zeta=b} - f(\zeta)|_{\zeta=c} \quad (32)$$

where

$$f(\zeta) \equiv \frac{\epsilon_0 L}{4\beta^4} V_p^2 \left( \frac{\hat{g}_0(18\zeta^2\beta^2 - 27\zeta\beta\hat{g}_0 + 11\hat{g}_0^2)}{(-\zeta\beta + \hat{g}_0)^3} + 6\ln(-\zeta\beta + \hat{g}_0) + \frac{\hat{g}_0(18\zeta^2\beta^2 + 27\zeta\beta\hat{g}_0 + 11\hat{g}_0^2)}{(-\zeta\beta - \hat{g}_0)^3} - 6\ln(\zeta\beta + \hat{g}_0) \right).$$

As done for equation (11), the solution of (31) can be obtained from series of successive approximation, see [16]. After some manipulation and under the assumption of very high  $Q$ -factor ( $B = 0$ ) the actual value of angular frequency assumes the expression:



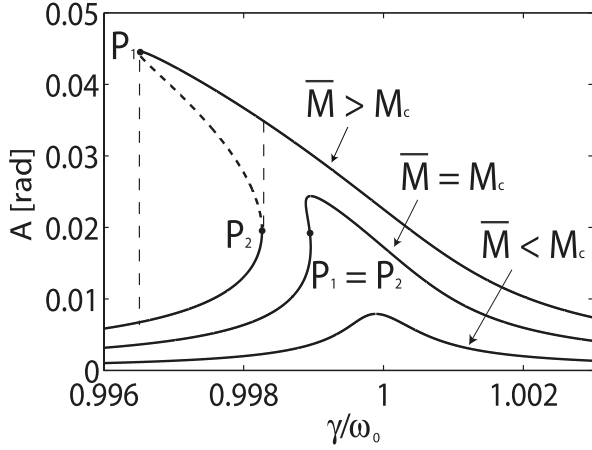


**Figure 7.** Frequency-response curves at varying dynamic excitation  $\bar{M}$ : stable response (continuous curves), unstable response (dashed curve) and hysteresis loop (thin dotted lines).

$$\omega = \omega_0 \left[ 1 + \left( \frac{3}{8} \frac{k_3}{k_1} - \frac{5}{12} \left( \frac{k_2}{k_1} \right)^2 \right) A^2 \right]. \quad (33)$$

The amplitude of the oscillation response driven by a harmonic momentum  $M(t) = \bar{M} \cos(\gamma t)$ , near the resonance ( $|\gamma - \omega|$  small) is given by the following nonlinear equation:

$$\left( \frac{\bar{M}}{k_1} \right)^2 = \left( 2 \left( 1 - \frac{\gamma}{\omega_0} \right) A + \left( \frac{3k_3}{4k_1} - \frac{5}{6} \left( \frac{k_2}{k_1} \right)^2 \right) A^3 \right)^2 + \left( \frac{B}{j\omega_0} A \right)^2. \quad (34)$$

It is worth noting that the second-order term always introduces a further ‘soft spring effect’, thus increasing the deviation of the resonance curve from the one of the linear problem. Figure 5 shows the resonance curves obtained: (i) neglecting nonlinearities; (ii) including the nonlinear third-order term; (iii) including both second- and third-order terms. In both cases (ii) and (iii) the resonance curve is bent towards the low frequencies and there can be three solutions in a certain frequency range, as shown in figure 7. Two solutions are stable while the third belongs to an unstable branch, dotted in figure 7. In this range hysteresis behavior is observed in experiments, as will be shown in section 5.3.

However, due to the presence of damping, the response becomes a multi-valued function of the frequency, only above a critical excitation amplitude  $M_c$ . Figure 7 shows typical responses for  $\bar{M} \lesseqgtr M_c$  in terms of oscillation amplitude  $A$ , versus normalized frequency  $\gamma/\omega_0$ . In all cases the resonant frequency is shifted backwards but for  $\bar{M} < M_c$  hysteresis phenomena due to the multi-valued response are avoided. Even though usually resonating devices are designed to have a hysteresis-free response, there are some applications in which the nonlinear bistable regime is attained, see e.g. [20]. The limit value  $M_c$  can be analytically evaluated by imposing the condition of existence of a single point with vertical tangent,  $P_1 \equiv P_2$  in figure 7, in the resonance curve  $A = A(\gamma)$  defined in equation (34), see [16] for details. One has

$$M_c^2 = \frac{8}{3} \frac{B^3 \omega_0^3}{|k_3|}. \quad (35)$$

## 5. Experimental results

### 5.1. Experimental set-up

To validate the model, several experimental measurements have been obtained on two torsional resonators belonging to the out-of-plane accelerometer built with the industrial surface micromachining process THELMA© from STMicroelectronics, see figure 1. The main nominal dimensions and mechanical parameters are reported in table 1. The proof mass of the accelerometer was kept inclined with an angle  $\beta$  to obtain different initial gaps between the electrodes and the resonating mass for resonators A and B.

The tested devices are packaged at a pressure of  $10^2$  Pa with the wafer-to-wafer bonding technique. The MEMS are wire-bonded directly to an electronic board housing two transimpedance amplifiers to read the currents flowing out of the two resonators. Each amplifier is formed by an AD8615 from Analog devices, a 1.3 M $\Omega$  resistor that sets the transimpedance gain and a 500 fF capacitance to limit the low pass filtering bandwidth at 245 kHz. The direct bonding, instead of the use of a ceramic carrier, allows the minimization of the parasitic capacitances, in particular the feedthrough capacitance between the actuation and sensing electrodes, which is finally compensated analytically as described in [11]. A typical spectral response of the current before and after compensation is shown in figure 8. The experimental spectrum (green line with circle markers) is characterized by a positive peak of resonance representing the maximum of the curve followed by a negative peak. The latter is caused by stray capacitance placed in parallel to the circuit representing the MEMS resonator. From the measured data, the stray capacitance is evaluated to be around 21 fF for resonator A and 15 fF for resonator B.

The experimental transfer curves are obtained by using an HP4195A spectrum analyzer that reads the output of each transimpedance driving one resonator at a time, to avoid possible cross-talk between the two; the result is then acquired through a Labview program to automatize the measurement.

### 5.2. Process parameter identification

First of all, the linear response was investigated to identify the rotation of the accelerometer’s proof mass  $\beta$  and two parameters that are not precisely known in the design phase, which are: the  $Q$ -factor value and the actual over-etch (it is nominally 0.35  $\mu\text{m}$  for this process and this value is the one taken into account during the design).

These parameters were extracted from the shift of the resonance frequency for increasing polarization voltages of the proof mass. The resonance frequency was considered as the peak of the admittances of the resonator (after the mentioned feedthrough compensation), measured as the ratio of

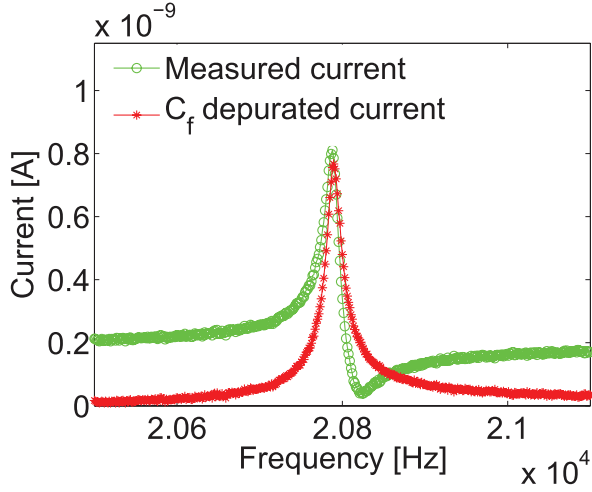


**Figure 8.** Spectral response of the torsional resonator B at  $V_p = 2.5$  V and  $|v_a| = 102$  mV before and after compensation.

the current flowing out from one electrode while a small oscillating voltage was applied to the other electrode.

Figures 9 and 10 show the results obtained in terms of frequency versus applied voltage  $V_p$  for the two resonators, respectively labeled A and B in figure 1. The points are the experimental data, the thick line represents the theoretical curve corresponding to the identified values of the over-etch, i.e.  $OE = 0.40 \mu\text{m}$ , and mass inclination, i.e.  $\beta = 4.85 \cdot 10^{-3}$  rad. The thin lines show the frequency variation for angle  $\beta$  varied of  $\pm 0.004$  rad with respect to the identified value and the dashed lines represent the frequency variation for over-etch varied of  $\pm 0.01 \mu\text{m}$ .

The experimental spectrum at very low excitation voltage, leading to a linear response, was used to identify the quality factor  $Q$ .

In order to compare the experimental results shown in term of current spectrum with the theoretical prediction (34), it is necessary to transform this spectrum in the  $\Theta$ -spectrum using the relation:

$$i(t) = V_p \frac{dC(\Theta(t))}{dt} \quad (36)$$

where  $C(\Theta(t))$  is the capacitance of the capacitor made by the oscillating mass and the sensing electrode. Referring to the torsional resonator in figure 3, the capacitance has the expression:

$$C(\Theta(t)) = \int_{-b}^{-c} \frac{\epsilon_0 L}{\hat{g}_0 + \beta y + \Theta(t)y} dy. \quad (37)$$

Substituting (37) into (36) an expression for the  $i(t)$  can be computed

$$i(t) = V_p \int_{-b}^{-c} -\frac{\epsilon_0 L}{(\hat{g}_0 + \beta y + \Theta(t)y)^2} dy \dot{\Theta}(t). \quad (38)$$

Under the hypothesis of small  $\Theta(t)$ , equation (38) can be linearized and Fourier transformed in order to obtain the  $\Theta$ -spectrum.

Figure 11 shows the experimental  $\Theta$ -spectrum thus obtained and the theoretical prediction with the identified value of

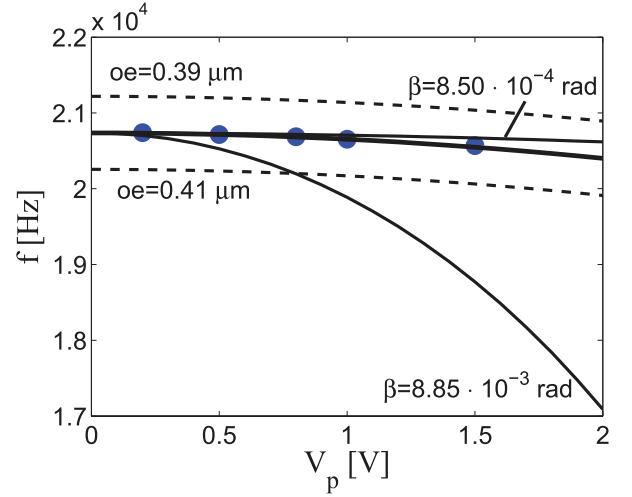


**Figure 9.** Resonance frequency as a function of the bias voltage: experimental data (blue dots) and theoretical predictions of the torsional resonator labeled A in figure 1.

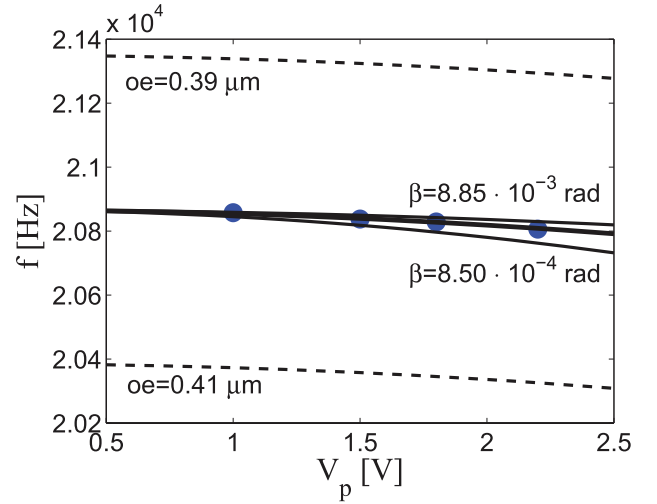


**Figure 10.** Resonance frequency as a function of the bias voltage: experimental data (blue dots) and theoretical predictions of the torsional resonator labeled B in figure 1.

the quality factor  $Q = 1080$  (see the thick line in figure 11). The value obtained by the approximate equation (29) for the same resonator, at a nominal pressure of  $10^2$  Pa, is  $Q_{FM} = 787$ . As expected, the real quality factor is higher than the one obtained through equation (29) due to the presence of holes in the mass.

**Remark.** In section 2 Hamilton's principle was applied to the simple torsional resonator of figure 4 with elongated springs, without folds. On the contrary, the real torsional resonator of the  $z$ -axis accelerometer shown in figure 1 is characterized by the presence of folded torsional springs. A COMSOL MULTIPHYSICS® numerical model was developed in order to calculate a corrective factor for the mechanical stiffness caused by the presence of the folds. Comparing the torque obtained with the FEM simulation to the torque obtained for the elongated torsional spring, a mechanical stiffness corrective factor of 1.39 was calculated. This factor was used for correcting the theoretical mechanical stiffness in the above comparison with experimental data.

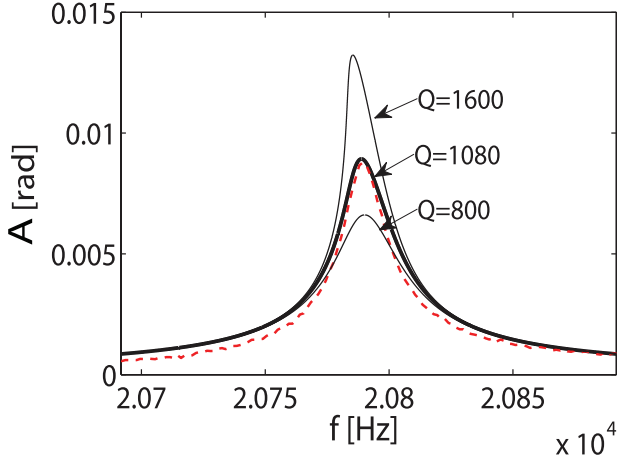


**Figure 11.** Experimental linear  $\Theta$ -spectrum is used to estimate the  $Q$ -factor of the device. The dashed line is the experimental  $\Theta$ -spectrum, the thin lines are the theoretical predictions at different  $Q$  values.

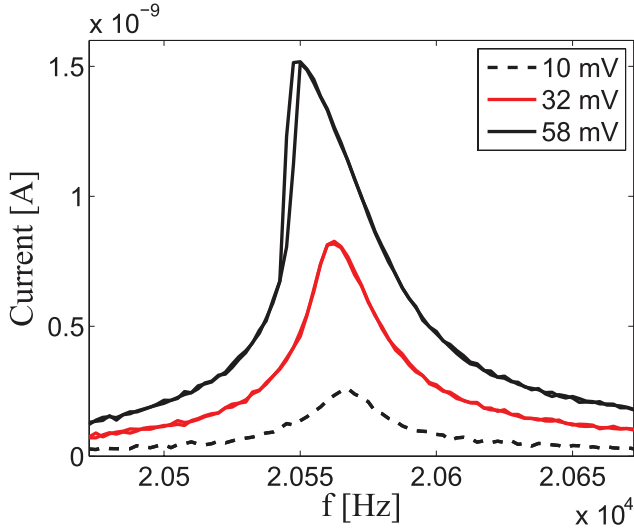


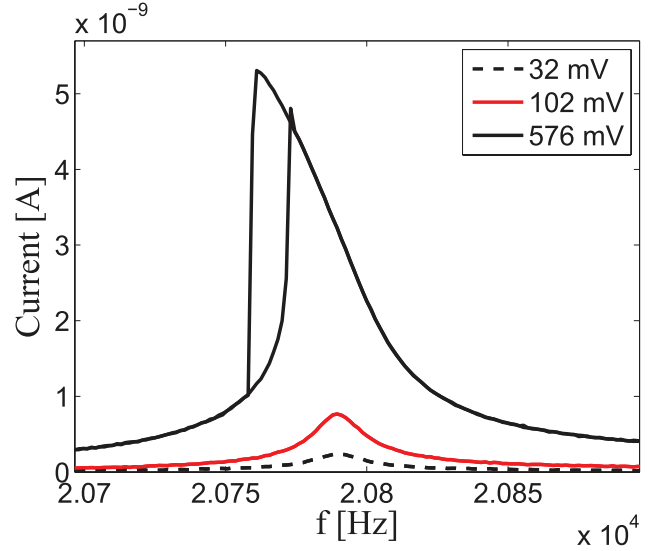
**Figure 12.** Current spectrum of the torsional resonator labeled A in figure 1 at  $V_p = 1.5$  V for different actuation voltage  $v_a$ .

### 5.3. Nonlinearities evaluation

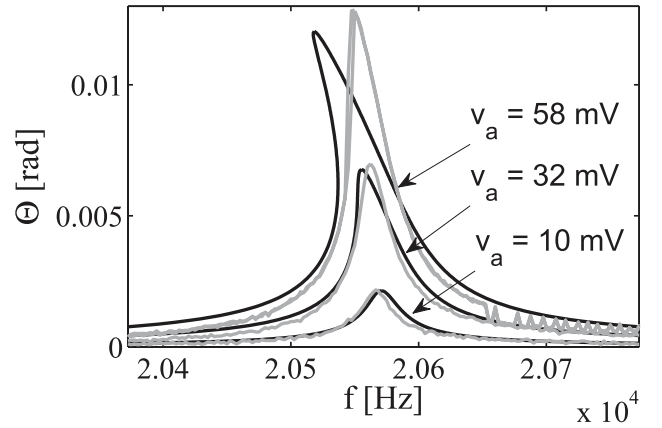
To analyze the nonlinear response, further measurements have been performed with increasing actuation voltages.

Figure 12 displays the current spectrum of the torsional resonator labeled A in figure 1 at the polarization voltage  $V_p = 1.5$  V for different actuation voltage  $v_a$ , while figure 13 shows the current spectrum of the torsional resonator labeled B in figure 1 at the polarization voltage  $V_p = 2.5$  V for different actuation voltage  $v_a$ . Note that different polarization voltages were used in order to obtain similar current values for the two resonators which have different rest gaps from the electrodes.

In both the resonators, as the driving actuation voltage increases, a soft spring effect is visible. Back-and-forth curves are shown which evidence hysteresis behavior for high actuation voltage. The critical value above which the hysteresis occurs can be analytically predicted using equation (35). For resonator A one obtains  $|v_a| = 40$  mV and for resonator B  $|v_a| = 315$  mV. These values are in agreement with the experimental results: for resonator A no hysteresis is observed at  $|v_a| = 10$  mV and



**Figure 13.** Current spectrum of the torsional resonator labeled B in figure 1 at  $V_p = 2.5$  V for different actuation voltage  $v_a$ .



**Figure 14.** Spectral response of the torsional resonator labeled A in figure 1 at  $V_p = 1.5$  V, for different actuation voltages  $v_a$ : comparison between experiments (gray lines) and theoretical prediction (black lines).

32 mV while hysteresis is present at  $|v_a| = 58$  mV, for resonator B no hysteresis is observed at  $|v_a| = 32$  mV and 102 mV while hysteresis is present at  $|v_a| = 576$  mV.

Comparing figure 12 with figure 13, one can observe that the nonlinear effect appears for lower applied voltage in resonator A due to the initial inclination of the proof mass and hence the reduced rest gap.

In figure 14 the theoretical and experimental results in terms of rotation versus frequency at  $V_p = 1.5$  V for the resonator labeled A in figure 1 are plotted at three different values of  $v_a$ : 10 mV, 32 mV and 58 mV.

In figure 15, instead, the theoretical and experimental results in terms of rotation versus frequency at  $V_p = 2.5$  V for the resonator labeled B in figure 1 are plotted at three different values of  $v_a$ : 32 mV, 102 mV and 576 mV.

A reasonably good agreement between prediction and experimental data is obtained in all cases.

**Remark.** With the actuation scheme of the resonator adopted, see figure 3, the electrostatic torque is proportional to the



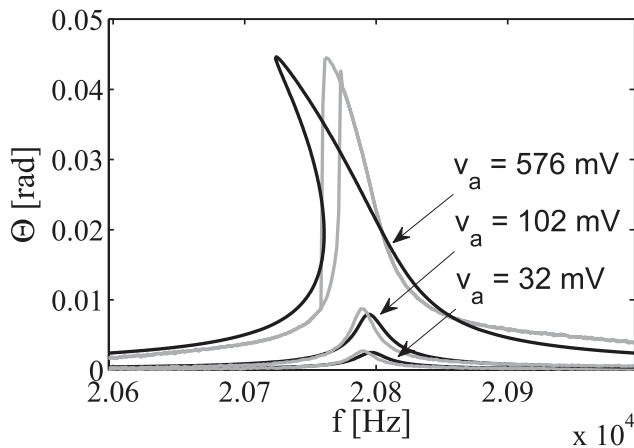


**Figure 15.** Spectral response of the torsional resonator labeled B in figure 1 at  $V_p = 2.5$  V, for different actuation voltages  $v_a$ : comparison between experiments (gray lines) and theoretical prediction (black lines).

actuation voltage and hence it oscillates with a very small magnitude, at least one order of magnitude below the limit of static pull-in calculated in [3] or of dynamic pull-in under a step actuation voltage, as calculated in [21]. However, the maximum amplitude of the angles reached by the two resonators are quite large since they are operating at resonance. For an accurate theoretical estimate of the pull-in in resonating conditions, a complete nonlinear dynamic analysis would be required as done in [22] for bending resonators. No dynamic pull-in was observed experimentally at the employed values of  $V_p$  and  $v_a(t)$ .

## 6. Conclusion

Starting from Hamilton's variational principle, a complete model for the description of the nonlinear dynamic behavior of an electrostatically actuated torsional resonator has been developed in this work. The model includes second-order and third-order terms arising from the electrostatic actuation and sensing. The role of the geometry of the oscillating mass in the nonlinear behavior is highlighted. The model, validated through comparison with experimental results obtained in this work on the resonant parts of a new out-of-plane accelerometer, provides a simple analytical tool that can be conveniently used in the design phase.

## Acknowledgments

This work has been partially funded by Eniac joint undertaking project Lab4MEMS, grant no. 325 622.

## References

- [1] Lee B, Oh C, Lee S, Oh Y and Chun K 2000 A vacuum packaged differential resonant accelerometer using gap sensitive electrostatic stiffness changing effect *Proc. 13th Ann. Int. Conf. MEMS (Miyazaki, Japan, Jan. 2000)* pp 352–7
- [2] Kim H C, Seok S, Kim I, Choi S-D and Chun K 2005 Inertial-grade out-of-plane and in-plane differential resonant silicon accelerometers (DRXLs) *13th Int. Conf. Solid-State*

- Sensors, Actuators and Microsystems (Transducers): Digest of Technical Papers (Seoul, Korea, Jun. 2005)* pp 172–5
- [3] Comi C, Corigliano A, Ghisi A and Zerbini S 2013 A resonant micro accelerometer based on electrostatic stiffness variation *Meccanica* **48** 1893–900
- [4] Comi C, Corigliano A and Baldassarre L 2014 Acceleration, angular velocity resonant detection integrated structure and related MEMS sensor device US *Patent Application* No. US 20140090469 A1
- [5] Li M, Rouf V T, Jaramillo G and Horsley D A 2013 MEMS Lorentz force magnetic sensor based on a balanced torsional resonator *Proc. 17th Int. Conf. on Solid-State Sensors, Actuators and Microsystems, Transducers and Eurosensors (Transducers and Eurosensors XXVII) (Barcelona, Spain, Jun. 2013)* pp 66–9
- [6] Charandabi S C, Muhammad H B, Anthony C J and Prewett P D 2012 Development of a torsional paddle microresonator for mass detection *Proc. 12th IEEE Conf. Nanotechn. (Birmingham, UK, Aug. 2012)* pp 1–5
- [7] Pandey A K, Pratap R and Chau F S 2008 Effect of pressure on fluid damping in MEMS torsional resonators with flow ranging from continuum to molecular regime *Exp. Mech.* **48** 91–106
- [8] Sung S, Lee J and Kang T 2003 Development and test of MEMS accelerometer with self-sustained oscillation loop *Sensors Actuators* **109** 1–8
- [9] Nguyen C T-C and Howe R T 1999 An integrated CMOS micromechanical resonator high- $Q$  oscillator *J. Solid-State Circuits* **34** 440–5
- [10] Kaajakari V, Mattila T, Oja A and Seppä H 2004 Nonlinear limits for single-crystal silicon microresonators *J. Microelectromech. Syst.* **13** 715–24
- [11] Tocchio A, Comi C, Langfelder G, Corigliano A and Longoni A 2011 Enhancing the linear range of MEMS resonators for sensing applications *IEEE Sensors J.* **11** 3202–10
- [12] Agarwal M, Park K K, Candler R N, Kim B, Hopcroft M A, Chandorkar S A, Jha C M, Melamud R, Kenny T W and Murmann B 2014 Nonlinear characterization of electrostatic MEMS resonators *Proc. MEMS (San Francisco, USA, Jan. 2014)*
- [13] Antonio D and Pastoriza H 2009 Nonlinear dynamics of a micromechanical torsional resonator: analytical model and experiments *J. Microelectromech. Syst.* **18** 1396–400
- [14] Corigliano A, Masi B D, Frangi A, Comi C, Villa A and Marchi M 2004 Mechanical characterization of polysilicon through on chip tensile tests *J. Microelectromech. Syst.* **13** 200–19
- [15] Clough R W and Penzien J 1993 *Dynamics of Structures* New York: McGraw Hill
- [16] Landau L D and Lifshitz E M 1965 *Meccanica* (Torino: Boringhieri)
- [17] Minikes A, Bucher I and Avivi 2005 Damping of a micro-resonator torsion mirror in rarefied gas ambient *J. Micromech. Microeng.* **15** 1762–9
- [18] Bao M, Yang H, Yin H and Sun Y 2002 Energy transfer model for squeeze-film air damping in low vacuum *J. Micromech. Microeng.* **12** 341–6
- [19] Frangi A, Ghisi A and Coronato L 2009 On a deterministic approach for the evaluation of gas damping in inertial MEMS in the free-molecule regime *Sensors Actuators A: Phys.* **149** 21–8
- [20] Almog R, Zaitsev S, Shtempluck O and Buks E 2007 Signal amplification in a nanomechanical Duffing resonator via stochastic resonance *Appl. Phys. Lett.* **90** 013508
- [21] Nielson G N and Barbastathis G 2006 Dynamic pull-in of parallel-plate and torsional electrostatic MEMS actuators *J. Microelectromech. Syst.* **15** 811–21
- [22] Nayfeh A H, Younis M I and Abdel-Rahman E M 2007 Dynamic pull-in phenomenon in MEMS resonators *Nonlinear Dyn.* **48** 153–63